Received 28 April 2007
Revised 9 April 2008
Accepted 21 April 2008

Non-equilibrium viscous shock-layer technique for computing hypersonic flow around blunt-nosed slender bodies

S. Ghasemloo and M. Mani
Center of Excellence in Computational Aerospace Engineering, Department of Aerospace Engineering, Amirkabir University of Technology, Tehran, Iran

Abstract

Purpose – The purpose of this paper is to present a non-equilibrium viscous shock layer (VSL) solution procedure that considerably improves computational efficiency, especially for long slender bodies.

Design/methodology/approach – The VSL equations are solved in a shock oriented coordinate system. The method of solution is spatial marching, implicit, finite-difference technique, which includes coupling of the normal momentum and continuity equations. In the nose region, the shock shape is specified from an algebraic expression and corrected through global passes through that region. The shock shape is computed as part of the solution beyond the nose region and requires only a single global pass. For this study, a seven-species $(O_2, N_2, O, N, NO, NO^+, e^-)$ air model is used.

Findings – The present approach eliminates the need for initial shock shape, which was required by previous method of solution. This method generates its own shock shape as a part of solution and the input shock shape obtained from a different solution is not required. Therefore, in comparison with the other VSL methods, the present approach dramatically reduces the CPU time of calculations. Moreover, by using the shock oriented coordinate systems the junction point problem in sphere-cone configurations is solved.

Practical implications – This method is an excellent tool for parametric study and preliminary design of hypersonic vehicles.

Originality/value – The present method provides a computational capability which reduces the CPU time, and expands the range of application for the prediction of hypersonic heating rates.

Keywords Aerodynamics, Heating, Viscosity, Equilibrium methods, Hypersonic flow
Paper type Research paper

Nomenclature

c_i = mass fraction of species i, ρ_i/ρ

C_p = specific heat at constant pressure, $C_P^*/C_{P\infty}^*$

h = static enthalpy, h^*/V_∞^{*2}

h_1, h_3 = metrics

J_i = diffusion mass flux of species i, $J_i^* R_n^*/\mu_{ref}$

k = thermal conductivity, $k^*/\mu_{ref}^* C_{P\infty}^*$

$k_{i,w}$ = surface reaction rate coefficient, $k_{i,w}^*/V_\infty$

L_e = Lewis number

M = Mach number

M_i = molecular weight of species i

n_b = Shock standoff distance

N_s = number of reacting species

p = pressure, $p^*/\rho_\infty^* V_\infty^{*2}$

International Journal of Numerical Methods for Heat & Fluid Flow
Vol. 19 No. 5, 2009
pp. 574-594

0961-5539
DOI 10.1108/09615530910963535

Pr	= Prandtl number
q	= heat transfer rate, $q^*/\rho^* V_\infty^{*3}$
R_n	= body nose radius
R_u^*	= universal gas constant
r	= radius measured from axis of symmetry, r^*/R_n^*
s	= coordinate measured along the shock wave, s^*/R_n^*
T	= temperature, $T^* C_{P\infty}^*/V_\infty^2$
u	= velocity component tangent to the shock, u^*/V_∞^*
v	= velocity component normal to the shock, u^*/V_∞^*
x, r, ϕ	= cylindrical coordinate system
ε	= Reynolds number parameter, $(\mu_{ref}/\rho_\infty^* u_n^* R_n^*)^{1/2}$
Γ_b	= body angle
Γ_s	= shock angle
η_n	= normalized n coordinate, 1-n/n_b
μ	= viscosity, μ^*/μ_{ref}^*
ξ	= normalized s coordinate, ξ = s
ρ	= density, ρ^*/ρ_∞
γ	= catalytic recombination coefficient of species *i*
$\dot{\omega}$	= mass rate of formation of species i, $\dot{\omega} R_n^*/\rho_\infty^* V_\infty^*$

Subscript and superscript

b	= body value
i	= species index
s	= shock value
w	= wall value
∞	= Free stream condition
*	= dimensional quantities

I. Introduction

At re-entry speeds the temperature near a body becomes extremely high, especially in the stagnation region. The high temperature and high convective velocities relative to reaction times mean that chemical non-equilibrium effects can be significant. Therefore, the air in the shock layer dissociates and ionizes. These phenomena will change considerably the chemical composition of the air and this change will be extended along the body. Accurate aerothermodynamic predictions during this part of the reentry trajectory are essential for sizing both the thermal protection system and aerodynamic control surfaces. For an accurate description of the flowfield, one must account for these real gas effects. Also an accurate estimate of the ionization level is needed for radio communication purposes. Therefore, a flowfield model including finite-rate chemistry is required.

The calculation of hypersonic viscous flowfields past long slender axisymmetric blunt bodies is of prime interest to the designer of certain aerospace vehicles. Since simulation of the high-energy thermodynamic environment of earth entries in ground-based experimental facilities is difficult, accurate and reliable flowfield prediction capabilities must be developed for efficient and reliable design of reentry vehicle. The development of the high-speed digital computers made numerical techniques an attractive tool for solving complex flowfields. Three popular computational approaches for obtaining aerothermodynamics predictions on these classes of vehicles are to solve the Navier-Stokes (NS) equations (Olynick and Tiwari, 1996), Parabolized Navier-Stokes (PNS) equations (Bhutta and Lewis, 1991) or Viscous Shock-Layer (VSL) equations. For highest fidelity, solutions to the full Navier-Stokes equations would be required, but this is very time- consuming. The PNS equations can be solved using a space-marching technique instead of the time-marching procedure which is usually

employed for the NS equations. The principle difficulty in applying the PNS equations to the hypersonic vehicles is that commonly the algorithms cannot solve blunt-body flowfields, while most reentry vehicle designs incorporate blunted nose in order to reduce peak heating rates. In addition, the numerical solution of the PNS equations requires a substantial amount of computer time and storage. The extensive computer run times prevent these approaches (i.e. NS and PNS) from being used in the preliminary design environment.

The third approach is to employ the VSL equations. The VSL equations were developed by Davis (1970a) and yield a simplified set of governing equations that are uniformly valid through the shock layer. The VSL method can accurately predict the blunt-body flowfield for a small fraction of the computing time required by NS schemes. This choice is very desirable for the preliminary design process where a range of geometries and flow parameters must be analyzed.

Numerous computational schemes for the solution of the VSL equations have been investigated in the past. Blottner (1969) was the first to develop the VSL approach for a multicomponent reacting gas at the stagnation point. He was followed shortly thereafter by Davis (1970b), who solved the VSL equations for a binary reacting gas and included flow downstream of the stagnation point. Both these works treated the fully catalytic case. Miner and Lewis (1975) extended the method of Davis (1970a) to a seven-species mixture and applied both fully catalytic and non-catalytic boundary conditions. Scott (1985) modified the Miner and Lewis code to include finite-rate catalycity for oxygen and nitrogen recombination. Kim *et al.* (1983, 1984) developed a three-dimensional VSL code for non-equilibrium flow over the space shuttle and included surface catalytic effects. Based on Davis (1970b) analysis, Moss (1974) developed a code using the VSL equations for a multicomponent gas mixture with chemical equilibrium or non-equilibrium. The VSL method of Moss (1974) updated by coupling the normal momentum and continuity equations (Lee and Gupta, 1992), which made the method of Moss (1974) stable even for the massive blowing conditions.

In the previous methods, an initial shock shape was required to start the solution of VSL equations. This was obtained by various procedures (thin VSL, inviscid solution,. . .), each requiring considerable computational effort. Moreover, the shock shape extending to the entire length of the body is globally iterated. The initial shock shape generation and the global iterations over the entire length of the body required considerable computational effort and run time respectively. Riley (1992) developed a method to obtain the inviscid flowfield around the blunt bodies in which the shock shape was generated. Cheatwood and DeJarnette (1992) used the same method to solve the approximate viscous shock layer (AVSL) equations. It is noticed that AVSL is an AVSL technique whose governing equations are identical to those of the standard VSL technique except that Maslen′s pressure relation is substituted for the normal momentum equation. In the present work, this method was developed for solving the VSL equations in chemical non-equilibrium flow conditions.

The present approach generates its own shock shape as a part of solution and provides a smooth shock shape in subsonic and supersonic regions. Therefore, the input shock shape obtained from a different solution is not required. It eliminates the need for initial shock shape, which was required by previous method of solutions. Moreover, the global iterations are limited to the subsonic region which is small region in the hypersonic flow over the blunt bodies. The VSL equations are solved in a shock oriented (rather than the traditional body oriented) coordinate system. Note that the use of a body coordinate system introduces discontinuities in the solution of governing

equations associated with the surface curvature discontinuity, such as at the sphere-cone tangency point of a spherically blunted cone. Also, the first-order continuity and normal momentum equations are solved simultaneously and the Vigneron condition is employed for the streamwise pressure gradient in the subsonic nose region. For most reentry applications, the temperature in the shock layer is such that a seven-species reacting model with a single ionizing species represents the chemistry reasonably well. In the present work, seven species ionizing air is considered, and it is assumed that chemical reactions proceed at finite rate. The accuracy of the developed code is validated by comparing the computational results with other solutions and available experimental data.

II. Analysis

II.a Governing equations

The conservation equations employed in this analysis are the VSL equations for a blunt axisymmetric body at zero angle of attack. These equations are written in a shock-oriented coordinate system (s,n) where the s coordinate is tangent to the shock in the stream wise direction and n is the normal to the shock (see Figure 1). To facilitate the solution, the VSL equations are transformed to normalized coordinates (ξ,η_n). The non-dimensional forms of the VSL equations for non-equilibrium flow in a normalized shock oriented coordinate system are: global continuity:

$$\frac{\partial}{\partial\xi}(\rho u h_3) - \frac{dn_b}{d\xi}\frac{\eta_n - 1}{n_b}\frac{\partial}{\partial\eta_n}(\rho u h_3) - \frac{1}{n_b}\frac{\partial}{\partial\eta_n}(\rho v h_1 h_3) = 0 \tag{1}$$

ξ-momentum:

$$\rho\left[\frac{u}{h_1}\left(\frac{\partial u}{\partial\xi} - \frac{\eta_n - 1}{n_b}\frac{dn_b}{d\xi}\frac{\partial u}{\partial\eta_n}\right) - \frac{v}{n_b}\left(\frac{\partial u}{\partial\eta_n} + \frac{u}{h_1}\frac{\partial h_1}{\partial\eta_n}\right)\right] + \frac{1}{h_1}\left(\frac{\partial p}{\partial\xi} - \frac{\eta_n - 1}{n_b}\frac{dn_b}{n\xi}\frac{\partial p}{\partial\eta_n}\right)$$
$$= \frac{\varepsilon^2}{n_{b^2}}\left\{\frac{\partial}{\partial\eta_n}\left[\mu\left(\frac{\partial u}{\partial\eta_n} - \frac{u}{h_1}\frac{\partial h_1}{\partial\eta_n}\right)\right] + \mu\left(\frac{2}{h_1}\frac{\partial h_1}{\partial\eta_n} + \frac{1}{h_3}\frac{\partial h_3}{\partial\eta_n}\right)\left(\frac{\partial u}{\partial\eta_n} - \frac{u}{h_1}\frac{\partial h_1}{\partial\eta_n}\right)\right\} \tag{2}$$

n-momentum:

$$\rho n_b\left[\frac{u}{h_1}\frac{\partial v}{\partial\xi} - \left(\frac{v}{n_b} + \frac{u}{h_1}\frac{\eta_n - 1}{n_b}\frac{dn_b}{d\xi}\right)\frac{\partial v}{\partial\eta_n} + \frac{u^2}{h_1 n_b}\frac{\partial h_1}{\partial\eta_n}\right] - \frac{\partial p}{\partial\eta_n} = 0 \tag{3}$$

Energy:

$$\rho C_{pf}\left[\frac{u}{u_1}\left(\frac{\partial T}{\partial\xi} - \frac{\eta_n - 1}{n_b}\frac{dn_b}{d\xi}\frac{\partial T}{\partial\eta_n}\right) - \frac{v}{n_b}\frac{\partial T}{\partial\eta_n}\right] - \frac{u}{h_1}\left(\frac{\partial p}{\partial\xi} - \frac{\eta_n - 1}{n_b}\frac{dn_b}{n\xi}\frac{\partial p}{\partial\eta_n}\right)$$
$$+ \frac{v}{n_b}\frac{\partial p}{\partial\eta_n} = \frac{\varepsilon^2}{n_{b^2}}\left\{\frac{\partial}{\partial\eta_n}k\left(\frac{\partial T}{\partial\eta_n}\right) + k\frac{\partial T}{\partial\eta_n}\left(\frac{1}{h_1}\frac{\partial h_1}{\partial\eta_n} + \frac{1}{h_3}\frac{\partial h_3}{\partial\eta_n}\right)\right.$$
$$\left. + \mu\left(\frac{\partial u}{\partial\eta_n} - \frac{u}{h_1}\frac{\partial h_1}{\partial\eta_n}\right)^2\right\} + \frac{\varepsilon^2}{n_{b^2}}\frac{\mu Le_{12}}{p_r}\sum_{i=1}^{Ns} Cp_i\frac{\partial c_i}{\partial\eta_n}\frac{\partial T}{\partial\eta_n} - \sum_{i=1}^{Ns} h_i\dot{\omega}_i \tag{4}$$

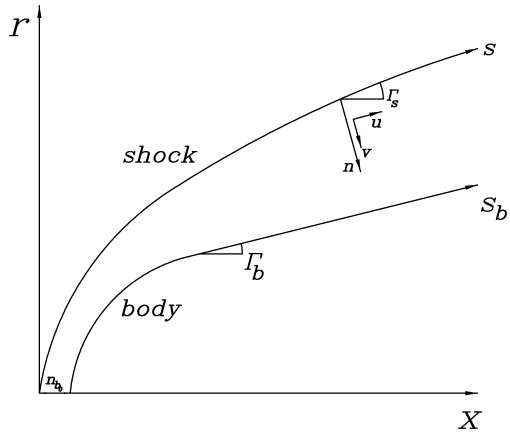

Figure 1.
Shock-oriented coordinate system

Species Continuity:

$$\rho\left[\frac{u}{h_1}\left(\frac{\partial c_i}{\partial \xi}-\frac{\eta_n-1}{n_b}\frac{dn_b}{d\xi}\frac{\partial c_i}{\partial \eta_n}\right)-\frac{v}{n_b}\frac{\partial c_i}{\partial \eta_n}\right]=\dot{\omega}_i+\frac{\varepsilon^2}{n_b^2 h_1 h_3}\frac{\partial}{\partial \eta_n}\left(h_1 h_3\frac{\mu Le_{12}}{p_r}\frac{\partial c_i}{\partial \eta_n}\right) \quad (5)$$

State:

$$P=\rho R_u T\sum_{i=1}^{Ns}\frac{c_i}{Mi} \quad (6)$$

II.b Boundary conditions

The boundary conditions at the shock are obtained by using the Rankine-Hugoniot relations. The flow behind the shock is assumed to be frozen at the freestream composition. No-slip boundary conditions are employed at the surface because the VSL equations in this study only simulate flight at lower altitudes. The wall conditions of chemical species are governed by catalytic relations on the wall and are obtained from the equation:

$$J_{i,w}-\frac{\rho k_{i,w}}{\varepsilon^2}c_i=0 \quad (7)$$

In the present work, three catalytic wall boundary conditions namely non-catalytic wall, fully catalytic wall, and finite-rate catalytic wall are used.

For a non-catalytic wall, the catalytic recombination rate is equal to zero (Gupta *et al.*, 1985), i.e.

$$\left(\frac{\partial c_i}{\partial \eta_n}\right)=0 \quad (8)$$

On the fully catalytic wall, the gas species are assumed to recombine to the freestream composition, i.e.

$$c_{i,w} = c_{i,\infty} \tag{9}$$

For the finite-catalytic wall, the catalytic recombination rate is expressed as

$$k_{i,w} = \sqrt{\frac{R_u^* T_w^*}{2\pi M_i^*}}\gamma_i \tag{10}$$

In the present study, according to Gupta (1996), the recombination coefficient for oxygen atom γo is given as

$$\gamma_O = 8.0\exp(-8600/T_w^*) \tag{11}$$

The recombination coefficient for nitrogen is the same as that employed by Scott (1981):

$$\gamma_N = 0.00714\exp(-2219/T_w^*) \tag{12}$$

The mass concentrations for other minor species including NO are set to be zero.

II.c Thermodynamic and transport properties

Thermodynamic properties for specific heat and enthalpy and transport properties for viscosity and thermal conductivity are required for each species considered. Values for the thermodynamic and transport properties are obtained by using curve fits give in Thompson *et al.* (1990). The mixture viscosity is obtained by using the Wilke's (1950) semi-emperical relation, and the mixture thermal conductivity is calculated using the formula of Mason and Saxena (1958). A constant Lewis number of 1.4 is used, and a variable Prandtl number is computed.

II.d Shock shape

In the present approach, the shock shape is generated as part of the solution. The shock shape is calculated based upon the method which is presented in Riley (1992). As mentioned earlier, the subsonic-transonic region is elliptic in nature, therefore, a marching scheme is not well posed. Thus, the complete shock shape for the entire subsonic-transonic region must be determined iteratively. A marching procedure is then used downstream of the subsonic-transonic region where the inviscid layer is supersonic. Generally, the three-dimensional shock surface in the subsonic-transonic region can be represented by three longitudinal conic sections blended in the circumferential direction with an ellipse as:

$$r = f(x, \phi) \tag{13}$$

Where (x, r, ϕ) are cylindrical coordinates. The x axis is aligned with the freestream velocity vector and is normal to the shock surface at the origin. Also $f(x,\phi)$ is defined as

$$f^2\left[B(x)\cos^2(\phi) + \sin^2(\phi)\right] + fC(x)\cos(\phi) = D(x) \tag{14}$$

in which

$$B(x) = \frac{f_2^2}{f_1 f_3}; \quad C(x) = B(x)(f_3 - f_1); \quad D(x) = f_2^2$$

Note that $f(x,\phi)$ is the radial coordinate of the three-dimensional shock surface in shock cylindrical coordinate system. The equation of the longitudinal conic sections is given by

$$f_k^2 + b_k x^2 - 2c_k x + 2d_k x f_k = 0 \ , k = 1, 2, 3 \tag{15}$$

Where k represents shock profiles for $\phi = 0°$, $90°$ and $180°$, respectively. The shock shape, defined above includes nine parameters of b_k, c_k and d_k where $k = 1,2,3$. For an axisymmetric flow, the total number of parameters governing the shock surface is reduced to b_1 and c_1 (Riley, 1992). The global iteration of the shock surface in the subsonic region involves matching the shape computed from the VSL equations to the actual body geometry. To insure a good starting solution for the downstream marching procedure, the matching body points are located at the end of the subsonic region where the inviscid layer is supersonic. Note that in this procedure flowfield is also solved behind the shock wave. At first, initial values are guessed for the above two parameters. The appropriate initial shock shape is produced by the values of 0.98 and 1.2 for b_1 and c_1. Since the initial shock shape (and the resulting jump condition) is known, the governing equations can be solved for the entire subsonic to obtain the calculated shock layer thickness, n_b, for all stations. The calculated thickness can be determined from the continuity equation:

$$\left(\frac{\cos\Gamma_s}{r_s^2}\int_0^1 \rho u(\eta_n - 1)d\eta_n\right)n_b^2 + \left(\frac{1}{r_s}\int_0^1 \rho u d\eta_n\right)n_b - \frac{1}{2} = 0 \tag{16}$$

The values for the calculated shock layer thickness at the two stations near the end of the subsonic region are compared with the values dictated by the geometry. Based on calculated and geometric shock layer thickness, new values of shock shape parameters b_1 and c_1 are computed. With each variation of these two parameters, the flowfield is solved for the entire subsonic region. This procedure is repeated until the calculated values of n_b at these two stations match to the geometric values. Downstream of this region, the shock shape is calculated through a marching scheme requiring no global iterations. For the supersonic region, the shock shape at the current station is described by a truncated Taylor's series (Cheatwood and DeJarnette, 1992).

$$r_s = r_{s_{i-1}} + \Delta x_s\left(\frac{dr_s}{dx_s}\right)_{i-1} + \frac{\Delta x_s^2}{6}\left[2\left(\frac{d^2 r_s}{dx_s^2}\right)_{i-1} + \left(\frac{d^2 r_s}{dx_s^2}\right)_i\right] \tag{17}$$

Where the shock slope is given by

$$\frac{dr_s}{dx_s} = \left(\frac{dr_s}{dx_s}\right)_{i-1} + \frac{\Delta x_s}{2}\left[\left(\frac{d^2 r_s}{dx_s^2}\right)_{i-1} + \left(\frac{d^2 r_s}{dx_s^2}\right)_i\right] \tag{18}$$

In these equations, the only unknown is the second derivative of r_s with respect to x_s (which is proportional to the shock curvature) at the current station. The initial value

for this parameter is calculated by linear extrapolation of its values at the previous two stations. Once the shock geometry and the corresponding jump conditions are constrained, the governing equations are solved. Then the calculated and the geometric values of n_b are compared to determine the error. Through successive application of the secant method (accompanied by a solution to the fluid equations), δ_{err} converges to a specified tolerance (1×10^{-4}). In summary, in the subsonic-transonic region, shock shape is specified from an algebraic relation and corrected through global iterations through that region. The shock shape is computed as part of the solution beyond the subsonic-transonic region. Thus, shock shape is not required as an input by the user.

II.e Method of solution

The method used for solving the full VSL equations is a spatial-marching, implicit, finite-difference method which includes coupling of the continuity and normal momentum equations. In the normalized shock-coordinate system (ξ,η_n), the conservation equation for streamwise momentum and energy can be written in the standard parabolic form:

$$A_0 \frac{\partial^2 W}{\partial \eta_n^2} + A_1 \frac{\partial W}{\partial \eta_n} + A_2 W + A_3 + A_4 \frac{\partial W}{\partial \xi} = 0 \tag{19}$$

where W represents the dependent variables u, T and, c_i, respectively. The coefficients A_0 through A_4 are non-linear coefficients. For the energy equation, the non-linearities are handled through a simple lagging technique. However, in order to speed convergence, the streamwise momentum equation is quasi-lineralized. In the finite-difference method used to solve the streamwise and energy equations, a two point backward differences is used for the derivatives with respect to ξ. The derivatives with respect to the η_n are replaced with three-point central differences. Replacing the differential terms by the finite-difference expressions, the governing equations are expressed as:

$$A_j W_{i,j-1} + B_j W_{i,j} + C_j W_{i,j+1} = D_j \tag{20}$$

Evaluating the coefficients of Equation (20) at discrete points across the shock layer along with the boundary conditions yields a tri-diagonal system of equations which may be solved using Thomas algorithm. The continuity and normal momentum equations are first order differential equations and, when solved independently, pose numerical difficulties. However, using the coupling approach, these two first equations are coupled together to form a second-order system that can be solved using Thomas algorithm. These equations are solved for the pressure and normal velocity. The density in these equations is eliminated by using the equation of state. The resulting equations are expressed in the finite-difference form at points (i,j + 1/2) and (i,j-1/2) using a box scheme. The final form for the continuity and normal momentum equations are:

$$\begin{aligned}
&A_{c,j+1/2} V_{i,j+1} + B_{c,j+1/2} V_{i,j} + C_{c,j+1/2} P_{i,j+1} + D_{c,j+1/2} P_{i,j} = E_{c,j+1/2} \\
&A_{c,j-1/2} V_{i,j} + B_{c,j-1/2} V_{i,j-1} + C_{c,j-1/2} P_{i,j} + D_{c,j-1/2} P_{i,j-1} = E_{c,j-1/2} \\
&A_{nm,j+1/2} V_{i,j+1} + B_{nm,j+1/2} V_{i,j} + C_{nm,j+1/2} P_{i,j+1} + D_{nm,j+1/2} P_{i,j} = E_{nm,j+1/2} \\
&A_{nm,j-1/2} V_{i,j} + B_{nm,j-1/2} V_{i,j-1} + C_{nm,j-1/2} P_{i,j} + D_{nm,j-1/2} P_{i,j-1} = E_{nm,j-1/2}
\end{aligned} \tag{21}$$

The coefficients of these equations are given in the Appendix. Eliminating P and V

alternatively in the coupled equations, two tridiagonal equations for pressure and normal velocity are obtained as:

$$A_p P_{i,j-1} + B_p P_{i,j} + C_p P_{i,j+1} = D_p \tag{22}$$

$$A_v B_{i,j-1} + B_v V_{i,j} + C_v V_{i,j+1} = D_v \tag{23}$$

Equations (22) and (23) are solved in the same way as the streamwise momentum, energy and species continuity equations. This numerical coupling enhances considerably the overall numerical stability of the VSL solution scheme. It is note to be that the shock standoff distance is evaluated by integrating the continuity equation.

The solution is started at the stagnation line. Using the stagnation line solution, the VSL equations are solved at the next down stream location by employing a two point backward-difference approximation for the streamwise derivative. The solution is iterated until the convergence is achieved. This procedure is repeated until a global solution at all locations is obtained. Note that the rate of production terms which are function of both T and c_i, appears in the species conservation and energy equations. For the species conservation equations, Blottner′s approach is used to linearize the production terms such that the species conservation appears as the only unknown. Furthermore, the production terms in the energy equation are also linearized such that the temperature appears as the only unknown. It is mentioned that at each location the equations are solved in the following order: The species conservation, energy and streamwise momentum equation are solved for c_i, T and u, respectively. The integration of the continuity equation determines the shock layer thickness, n_b. Then, the continuity and normal momentum equations are solved simultaneously for p and v. Finally, the density ρ is obtained using the equation of state.

III. Results and discussion

At the first step the present method is validated against experimental and the other VSL methods. Then the effect of catalytic wall on the surface quantities is studied using this method. Note that all variables are non-dimensionalized by reference quantities presented in nomenclature.

Figures 2 and 3 represent the result of the application of the method to STS-2 laminar heating and the results from the experiments from Shinn *et al.* (1982). An "equivalent axisymmetric body" concept was used in Shinn *et al.* (1982) to model the windward centerline of the shuttle at a given angle of attack with an appropriate axisymmetric body at zero angle of attack. The axisymmetric body is hyperboloid with nose radii R_n and asymptotic body half-angles θ_b as given in each figure. The results that are shown on each figure are the experimental data and present VSL predictions based on a finite-catalytic wall condition using k_w, based on Equation (10). In Figure 2, the surface heating rate for an altitude of 77.91 km are presented and are seen to compare well (generally within 20 per cent) with the experimental data. At 60.56 km altitude (Figure 3), the agreement between the predicted and measured heating value is quite good (within five percent). The heating rates of present method for 6°, 10° and 20° sphere-cones are compared with the VSL method by Lee and Gupta (1992) in Figures 4-6. Freestream conditions are for 53.34 km altitude and Mach number of 25.The bodies have the same nose radius which equals 0.0381 m. Both non-catalytic and fully catalytic surface are examined to show the limiting effects of wall catalycity

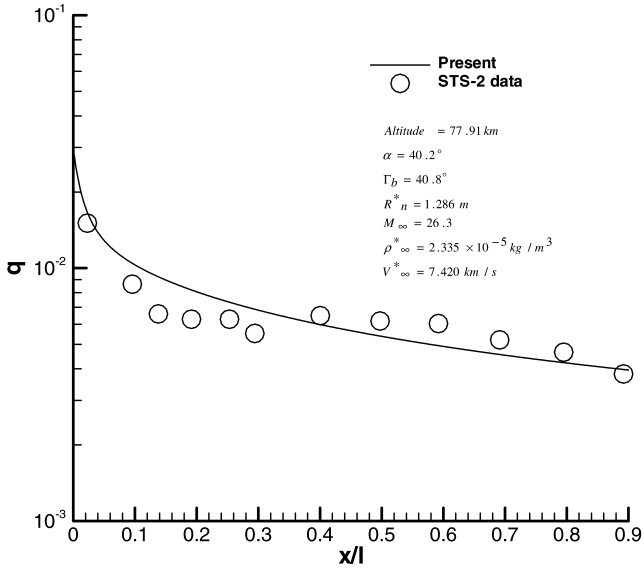

Figure 2.
Comparison of calculated and measured heating rates an altitude of 77.91 km

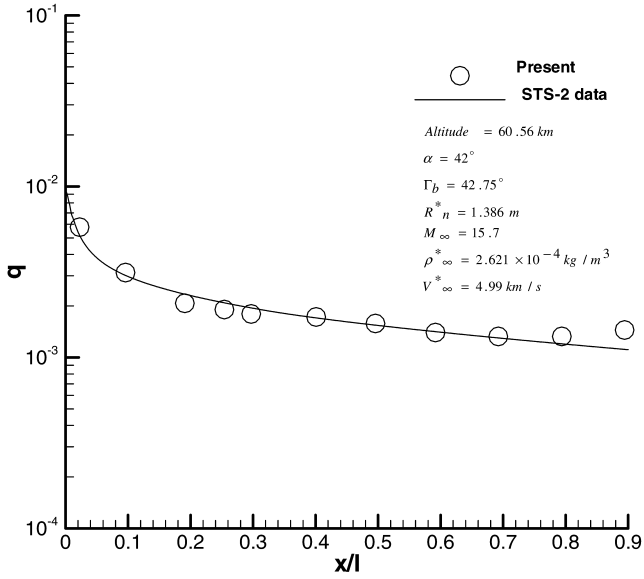

Figure 3.
Comparison of calculated and measured heating rates an altitude of 60.56 km

on heating. It should be mentioned that all calculations were done using 101 grid points between the body and the shock. The results of the present method are generally in good agreement (within four to fifteen percent) with the Lee method. In the ξ direction, the step size of 0.08 of R_n id used. In η_n direction, the nodes are made dense near the body. The above mentioned grid spacing are determined through the grid convergence study which will be presented completely at the end of this section. The computed

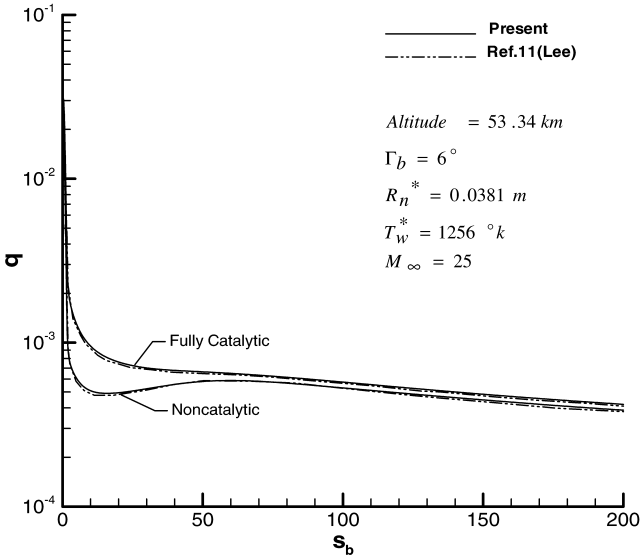

Figure 4.
Non-equilibrium heating rate comparison for 6° sphere-cone

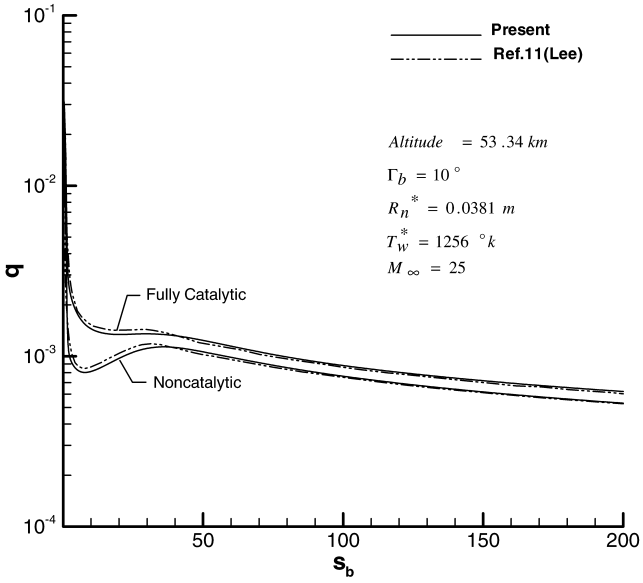

Figure 5.
Non-equilibrium heating rate comparison for 10° sphere-cone

heating rate for 6° sphere-cone show excellent agreement with the results by Lee, while the 20° sphere-cone shows a greater deviation. However, the maximum deviation (in the spherical region) was found to be fifteen percent. From these figures, it is seen that the heating rates with the non-catalytic surface may decrease more than 45 per cent in comparison to that with the fully catalytic surface on the spherical region. The differences in the heating rates decrease in the downstream region. Since globally iterated results have been demonstrated to be quite accurate, results obtained by the

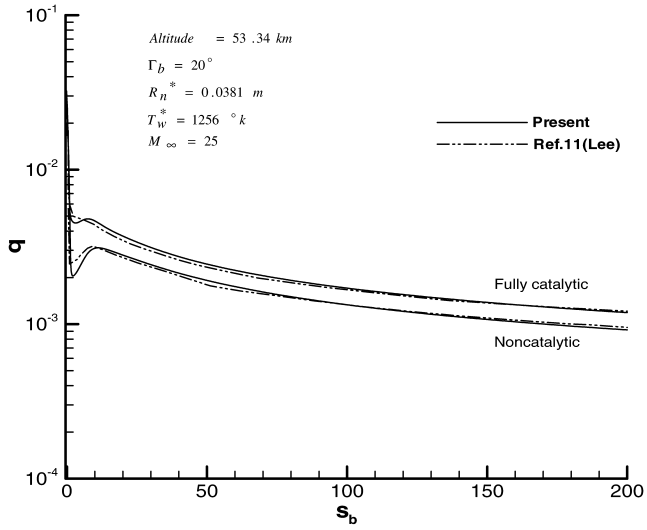

Figure 6.
Non-equilibrium heating rate comparison for 20° sphere-cone

present method are also considered equally good. The shock standoff distance for a 10° sphere-cone is shown in Figure 7. The results obtained from the present method are in good agreement with those obtained from the globally iterated technique. The electron concentration profiles for the RAM C 9° sphere-cone are shown in Figure 8. Predictions of electron concentration profiles for $S_b = 8.8$ are given for 70.104, 76.20, 80.772 and 83.820 km. The freestream velocity and wall temperature for these altitudes are 7,620 m/s and 1,000°k, respectively. In Figure 8, the calculated results are compared with the experimental data (Evans *et al.*, 1973). The present calculations agree

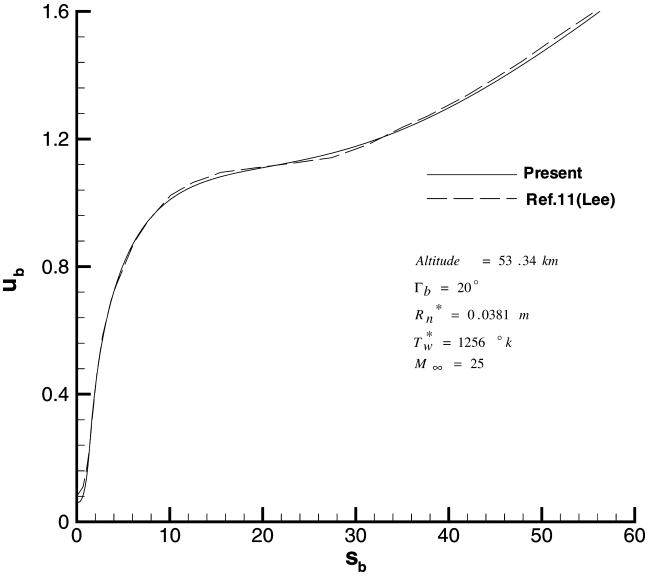

Figure 7.
Shock standoff distance comparison for 20° sphere-cone with non-equilibrium chemistry

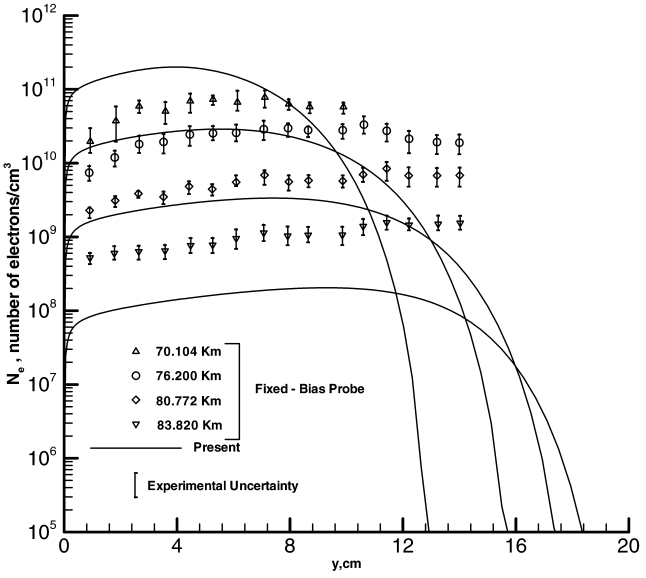

Figure 8.
Comparison of electron concentration profiles for RAM C

reasonably well with the experimental data as to level of ionization. The agreement between the present predictions and the experimental data is good at 70.104, 76.20 and 80.772 km, but at 83.82 km, the present method significantly underpredicted electron concentration. It is important to notice that the present results are for no slip conditions. It seems using the slip boundary condition will improve the results especially for altitude of 83.82 km. From these figures, it is concluded that the results of the present method are enough accurate against the results of experiments and other methods of solution.

After validating the present method with other predictions and experimental data, results for three sphere-cones with body half angles of 6°, 10° and 20° are now presented to illustrate the effects of body angle and surface catalysis.

The calculations are for a Mach number of 25 at an altitude of 53.34 km. The results for the ratio of surface heating rate with non-catalytic wall to that with fully catalytic wall are shown in Figure 9. This ratio demonstrates the maximum potential for a surface heating-rate reduction in the presence of dissociated non-equilibrium flow. The ratios keep decreasing up to the tangency point, then increase up to maximum value in the recompression region, and finally, decrease to a constant value on the far downstream region. For stations beyond 80 nose radii, the results indicate a greater potential for a heating reduction to the 20° cone than the corresponding to the 6 and 10° cones. As shown in Figures 10 and 11, these results can be attributed to a higher concentration of dissociated species present throughout the flowfield for energy transport by diffusion to the surface for the wider angle cone. In this body region for the lower cone angles, the necessary conditions to produce dissociated species exist only in a smaller region of the boundary layer. Figures 12 to 14 show the effects of body angle on the surface heating rates and surface pressure. Figures 12 and 13 represent the heating rates for a non-catalytic wall and for a fully catalytic wall, respectively. The surface pressure distributions are illustrated in Figure 14. As shown in Figure 14, the wall catalycity has negligible effect on the surface pressure. It is seen that the surface

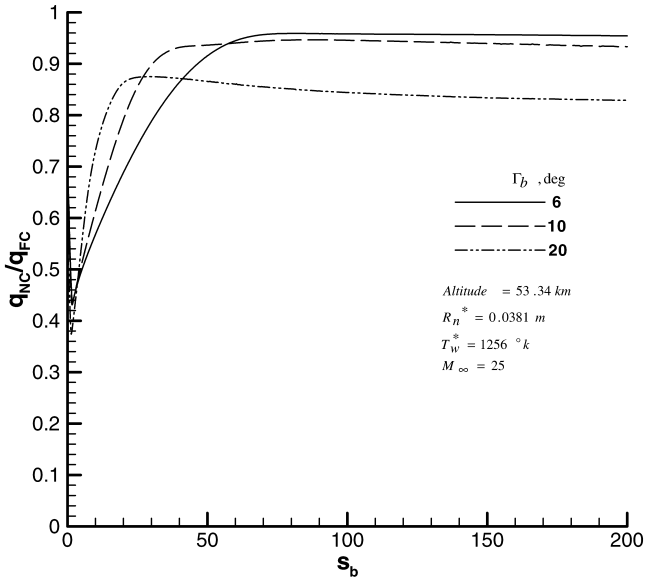

Figure 9.
Effect of body angle on non-catalytic to fully catalytic heating ratio

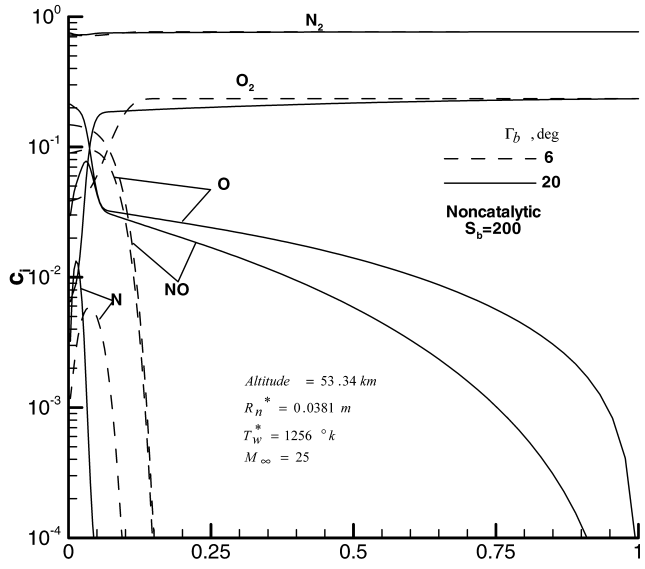

Figure 10.
Species concentration profiles for a non-catalytic wall

heating rate and surface pressure decreases as the half body angle decreases. Electron concentration profiles for the 6° sphere-cone are shown in Figure 15. The computations are performed for a fully catalytic wall. As mentioned earlier, the slip conditions are not considered in this study. Therefore, the species concentrations behind the shock are the same as in the freestream, and thus the concentrations of both NO+ and electrons are zero. The electrons are concentrated at the nose, and the concentration decrease in the s direction. Since the maximum temperature in the shock layer is near the shock, the

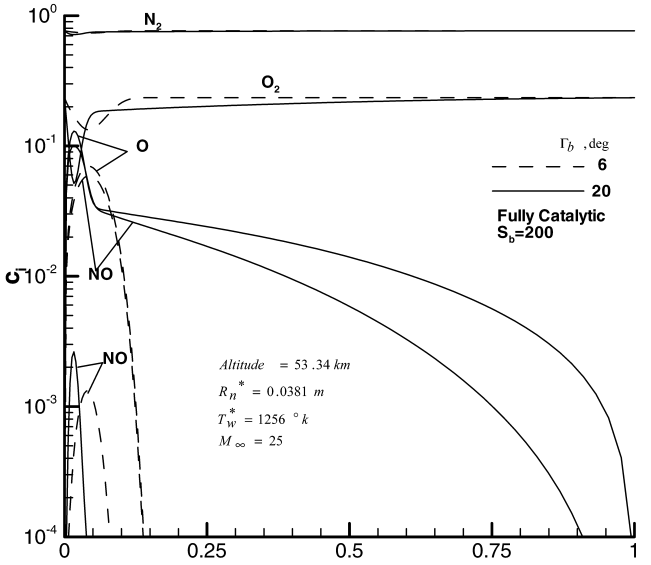

Figure 11.
Species concentration profiles for a fully catalytic wall

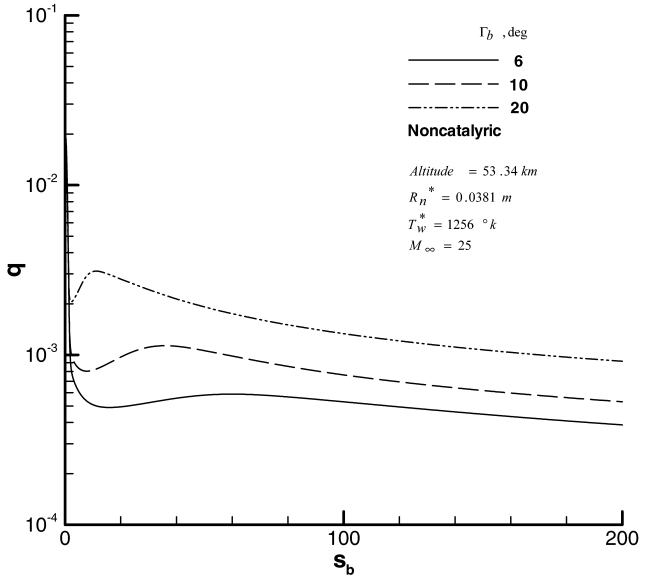

Figure 12.
Body angle effect on non-equilibrium heating rate with non-catalytic wall

electron density occurs in the shock layer and decreases toward the shock. The present method predicted this trend correctly.

A CPU time comparison between the results of present method and those of (Cheatwood and DeJarnette, 1992) is presented here. The computer used for this study includes a Pentium IV processor, and Ram of 512 Meg. The flowfield and the sphere-cone are the same as the one in Figure 6, however, the solution is marched up to 250 Rn

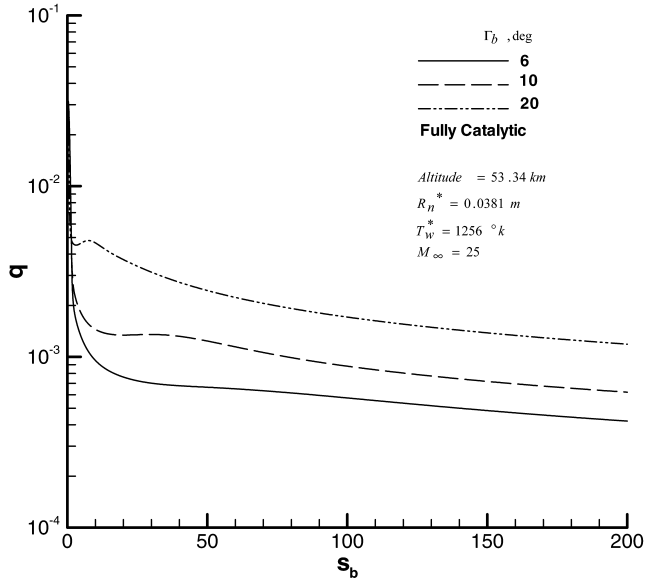

Figure 13.
Body angle effect on non-equilibrium heating rate with fully catalytic wall

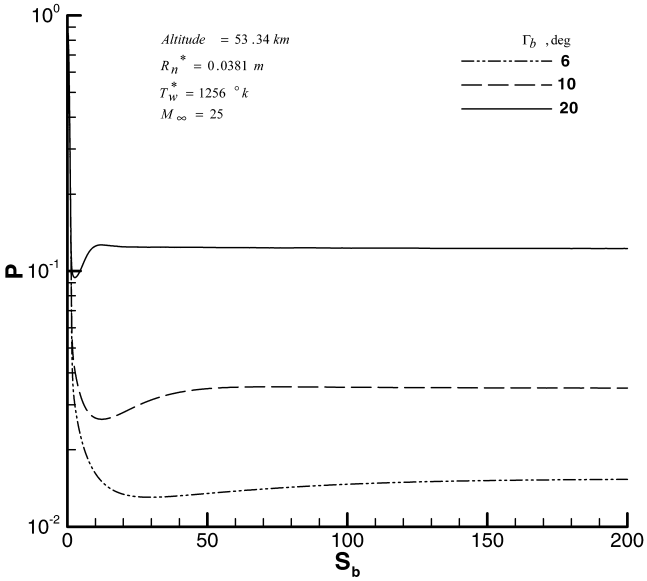

Figure 14.
Body angle effect on surface pressure

for this CPU time comparison. The results are shown in Table I. As was mentioned earlier a 65 per cent reduction in CPU time is obtained relative to method of (Swaminathan *et al.*, 1983). At the end, the grid convergence study is presented. According to Table II, for $\Delta\xi^*/Rn^* = 0.02$, the effect of various nodes in η_n direction is given through cases a.1 to a.6. As is seen in Figure 16, there are no differences between

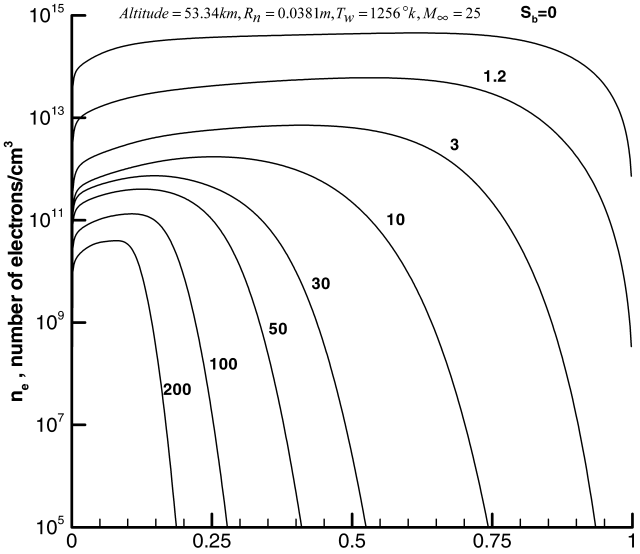

Figure 15.
Electron concentration profiles for 6° sphere-cone at 53.34 km

20° sphere-cone, R_N = 0.0381 m for length of 250 R_n				
	Sun sparcstation 1 +		Pentium IV	
	AVSL [13]	VSL [22]	AVSL [13]	VSL present
Station	157	587	157	587
CPU time (sec)	525	7,961	31	168
Grid pts/sec	15	4	258	178

Table I.
CPU time comparison

Cases	No. of nodes in η_n direction	$\Delta\xi^*/R_n^*$
a.1	31	0.02
a.2	51	0.02
a.3	71	0.02
a.4	81	0.02
a.5	91	0.02
a.6	101	0.02
b.1	101	0.04
b.2	101	0.06
b.3	101	0.08

Table II.
Grid specifications for turbulent cases

the a.5 and a.6 curves. Therefore 101 nodes in η_n direction is enough. Cases b.1 through b.3 demonstrates the effect of different $\Delta\xi$ values for fixed node number of 101 in direction η_n. As is seen in Figure 17, there is no differences between these results. Therefore a value of $\Delta\xi^* = 0.08\,R_n*$ is appropriate.

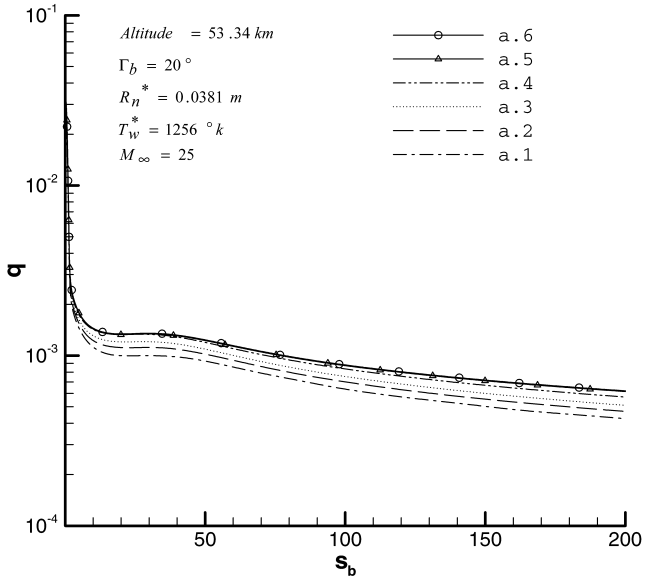

Figure 16.
Effect of number of nodes in η_n direction on the surface heat transfer distribution

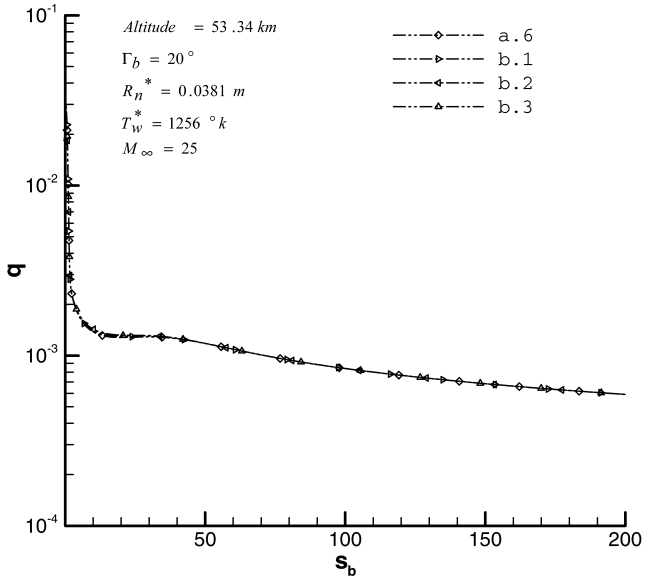

Figure 17.
Effect of $\Delta\xi$ on the surface heat transfer distribution

IV. Conclusions

A new technique to solve non-equilibrium VSL equations is proposed with increases computational efficiency. For this study, a seven-species air model is used and the chemical reaction model is taken from Blottner. In the present method, the initial shock shape is not required and the global iteration is confined merely to the nose region. The

shock shape is defined with an algebraic (conic) equation and is iterated globally in the nose region until the calculated body matches with the real body at the end of the subsonic region. In the supersonic region, the marching scheme is well posed. Hence, the shock shape and flow field can be determined in each station and there is no need for global iteration. Since the subsonic region is only a small portion of the flow field for hypersonic flows over slender bodies, and the global iteration is confined for this region only in the present method, a significant reduction in CPU time is achieved. Moreover, by using the shock coordinated systems the junction point problem in sphere-cone configurations is solved. Results of the present method compare quite favorably with experimental data and other predictions. Finally, we conclude that the present method provides a computational capability which reduces the CPU time, and expands the range of application for the prediction of hypersonic heating rates.

References

Bhutta, B.A. and Lewis, C.H. (1991), "Comparison of hypersonic experiments and PNS predictions", *Journal of Spacecraft and Rockets*, Vol. 28 No. 4, pp. 376-86.

Blottner, F.G. (1969), "Viscous shock layer at the stagnation point with nonequilibrium air chemistry", *AIAA Journal*, Vol. 7 No. 12, pp. 2281-87.

Cheatwood, F.M. and DeJarnette, F.R. (1992), "An approximate viscous shock layer technique for calculating nonequilibrium hypersonic flows about blunt-nosed bodies", AIAA-92-0498.

Davis, R.T. (1970a), "Hypersonic flow of a chemically reacting binary mixture past a blunt body", *AIAA*, Vol. 70-805.

Davis, R.T. (1970b), "Numerical solution of the hypersonic viscous shock layer equations", *AIAA Journal*, Vol. 8 No. 5, pp. 843-51.

Evans, J.S., Schexnayder, C.J., Jr. and Huber, P.W. (1973), "Boundary-layer electron profiles for entry of a blunt slender body at high attitude", NASA TN D-7332.

Gupta, R.N. (1996), "Reevaluation of flight-derived surface recombination-rate expression for oxygen and nitrogen," *Journal of Spacecraft and Rockets*, Vol. 33 No. 3, pp. 451-3.

Gupta, R.N., Scott, C.D. and Moss, J.N. (1985), "Slip-boundary equations for multicomponent nonequilibrium airflow", NASA TP-2452.

Kim, M.D., Swaminathan, S. and Lewis, C.H. (1983), "Three dimensional viscous flow over the shuttle with surface catalytic effects", AIAA-83-1426.

Kim, M.D., Swaminathan, S. and Lewis, C.H. (1984), "Three dimensional nonequilibrium viscous flow over the space shuttle orbiter", *Journal of Spacecraft and Rockets*, Vol. 21, pp. 29-35.

Lee, K P. and Gupta, R.N. (1992), "Viscous shock-layer analysis of hypersonic flows over long slender vehicles", NASA CR-189614.

Mason, E.A. and Saxena, S.C. (1958), "Approximate formula for the thermal conductivity of gas mixtures", *The Physic of Fluids*, Vol. 3 No. 5, pp. 361-9.

Miner, E.W. and Lewis, C.H. (1975), "Hypersonic ionizing air viscous shock-layer flows over nonanalytic blunt bodies", NASA CR-2550.

Moss, J.N. (1974), "Reacting viscous shock layer solutions with multicomponent diffusion and mass injection", NASA TR-R-411.

Olynick, D.R. and Tiwari S.B. (1996), "Navier-stokes heating calculations for benchmark thermal protection system sizing ", *Journal of Spacecraft and Rockets*, Vol. 33 No. 6, pp. 807-14.

Riley, C.J. (1992), "An Engineering method for interactive inviscid-boundary layers in three-dimensional hypersonic flows", PhD thesis, North Carolina State University, Raleigh, NC.

Scott, C.D. (1981), "Catalytic recombination of oxygen and nitrogen in high temperature reusable surface insulation", in Crosbie, A.L. (Ed.), *Aerothermodynamics and Planetary Entry*, Vol. 77, Progress in Astrodynamics and Aeronautics, AIAA, New York, NY, pp. 192-212.

Scott, C.D. (1985), "Effects of nonequilibrium and wall catalysis on space shuttle heat transfer", *Journal of Spacecraft and Rockets*, Vol. 22, pp. 489-99.

Shinn, J.L., Moss, J.N. and Simmonds, A.L. (1982), "Viscous-shock-layer heating analysis for the shuttle windward plane with surface finite catalytic recombination rates", AIAA-82-0842.

Swaminathan, S., Kim, M.D. and Lewis, C.H. (1983), "Three-dimensional nonequilibrium viscous shock-layer flows over complex geometries", AIAA Paper 83-0212.

Thompson, R.A., Lee, K.P. and Gupta, R.N. (1990), "Computer codes for the evaluation of thermodynamic properties, transport properties, and equilibrium constants of an 11-species air model", NASA TM-102602.

Wilke, C.R. (1950), "A viscosity equation for gas mixtures", *Journal of Chemical Physics*, Vol. 18 No. 4, pp. 517-9.

Appendix

The coefficients for Equations (20) are obtained as follows:

$$A_{c,j+1/2} = -\frac{(h_1 h_3)_{j+1/2}}{\Delta\eta_{n,j+1}}$$

$$B_{c,j+1/2} = \frac{(h_1 h_3)_{j+1/2}}{\Delta\eta_{n,j+1}}$$

$$C_{c,j+1/2} = \frac{n_b h_{3,j+1/2} u_{i,j+1/2}}{2\Delta\xi_i P_{i,j+1/2}} - \frac{h_{3j+1/2}}{\Delta\eta_{n,j+1} P_{i,j+1/2}}\left[(\eta_{n,j+1/2}-1)u_{i,j+1/2}\frac{dn_b}{d\xi} + h_{1_{j+1/2}} V_{i,j+1/2}\right]$$

$$D_{c,j+1/2} = \frac{n_b h_{3,j+1/2} u_{i,j+1/2}}{2\Delta\xi_i P_{i,j+1/2}} + \frac{h_{3j+1/2}}{\Delta\eta_{n,j+1} P_{i,j+1/2}}\left[(\eta_{n,j+1/2}-1)u_{i,j+1/2}\frac{dn_b}{d\xi} + h_{1_{j+1/2}} V_{i,j+1/2}\right]$$

$$\begin{aligned} E_{c,j+1/2} = {} & \frac{n_b h_{3,j+1/2} u_{i,j+1/2}}{2\Delta\xi_i P_{i,j+1/2}}(P_{i-1,j+1} + P_{i-1,j}) - \frac{n_b h_{3,j+1/2}}{2\Delta\xi_i}(u_{i,j+1} + u_{i,j} - u_{i-1,j+1} \\ & - u_{i-1,j} - \frac{u_{i,j+1/2}}{T_{i,j+1/2}} \times (T_{i,j+1} + T_{i,j} - T_{i-1,j+1} - T_{i-1,j})) - \frac{n_b u_{i,j+1/2}}{2\Delta\xi_i} \\ & \times [(h_3)_{i,j+1} + (h_3)_{i,j} - (h_3)_{i-1,j+1} - (h_3)_{i-1,j}] + V_{i,j+1/2}\left[(h_1)_{j+1/2}\left(\frac{\partial h_3}{\partial\eta_n}\right)_{j+1/2}\right. \\ & \left. + (h_3)_{j+1/2}\left(\frac{\partial h_1}{\partial\eta_n}\right)_{j+1/2}\right] - \frac{V_{i,j+1/2}(h_1 h_3)_{j+1/2}}{\Delta\eta_{n,j+1} T_{i,j+1/2}}[T_{i,j+1} - T_{i,j}] \\ & + \frac{n_b h_{3,j+1/2}(\eta_{n,j+1/2}-1)}{\Delta\eta_{n_{j+1}}}\left[u_{i,j+1} - u_{i,j} - \frac{u_{i,j+1/2}}{T_{i,j+1/2}}(T_{i,j+1} - T_{i,j})\right] \\ & + (\eta_{n,j+1/2}-1)u_{i,j+1/2}\frac{dn_b}{d\xi}\left(\frac{\partial h_3}{\partial\eta_n}\right)_{j+1/2} - \frac{u_{i,j+1/2} h_{3,j+1/2} n_b}{2\Delta\xi_i M_{i,j+1/2}} \end{aligned}$$

$$\times[M_{i,j+1}+M_{i,j}-M_{i-1,j+1}-M_{i-1,j}]+\frac{(h_1h_3)_{j+1/2}V_{i,j+1/2}}{\Delta\eta_{n,j+1}M_{i,j+1/2}}[M_{i,j+1}-M_{i,j}]$$

$$+\frac{u_{i,j+1/2}}{M_{i,j+1/2}\Delta\eta_{n,j+1}}\frac{dn_b}{d\xi}h_{3j+1/2}(\eta_{n,j+1/2}-1)[M_{i,j+1}-M_{i,j}]$$

$$A_{nm,j+1/2}=\frac{n_bP_{i,j+1/2}u_{i,j+1/2}}{2\Delta\xi_ih_{1,j+1/2}}-\frac{P_{i,j+1/2}}{\Delta\eta_{n,j+1}}\left[\frac{u_{i,j+1/2}(\eta_{n,j+1/2}-1)}{h_{1,j+1/2}}\frac{dn_b}{d\xi}+V_{i,j+1/2}\right]$$

$$B_{nm,i+1/2}=\frac{n_bP_{i,j+1/2}u_{i,j+1/2}}{2\Delta\xi_ih_{1,j+1/2}}+\frac{P_{i,j+1/2}}{\Delta\eta_{n,j+1}}\left[\frac{u_{i,j+1/2}(\eta_{n,j+1/2}-1)}{h_{1,j+1/2}}\frac{dn_b}{d\xi}+V_{i,j+1/2}\right]$$

$$C_{nm,j+1/2}=\frac{-R_uT_{i,j+1/2}}{M_{i,j+1/2}\Delta\eta_{n,j+1}}$$

$$D_{nm,j+1/2}=\frac{-R_uT_{i,j+1/2}}{M_{i,j+1/2}\Delta\eta_{n,j+1}}$$

$$Enm=\frac{n_bP_{i,j+1/2}u_{i,j+1/2}}{2\Delta\xi_ih_{1,j+1/2}}(V_{i-1,j+1}+V_{i-1,j})-\frac{u^2_{i,j+1/2}P_{i,j+1/2}}{h_{1,j+1/2}}\left(\frac{\partial h_1}{\partial\eta_n}\right)_{j+1/2}$$

Corresponding author
S. Ghasemloo can be contacted at: sghasemloo@aut.ac.ir